Supporting Information

All-solid-state lithium-oxygen batteries with high areal capacity and fast rate capability enabled by amorphous lithium peroxide

Shu-Ting Ko[a], Ziting Ma[a], Cruz Gonsalves[a], Karlo Adrian Salazar[a], Sarah Mellado[a], Chuck Chunhu Tan[b], Timothy Lin[b], Toshihiro Aoki[c], Chunting Chris Mi[d], and Lingping Kong[a,*]

[a] Department of Mechanical Engineering, San Diego State University, CA, 92182, USA

[b] Solid Energies, Inc. Anaheim, CA, 92801, USA

[c] Irvine Materials Research Institute, University of California, Irvine, CA, 92697, USA

[d] Department of Electrical and Computer Engineering, San Diego State University, CA, 92182, USA

[*] Corresponding author e-mail: lkong@sdsu.edu

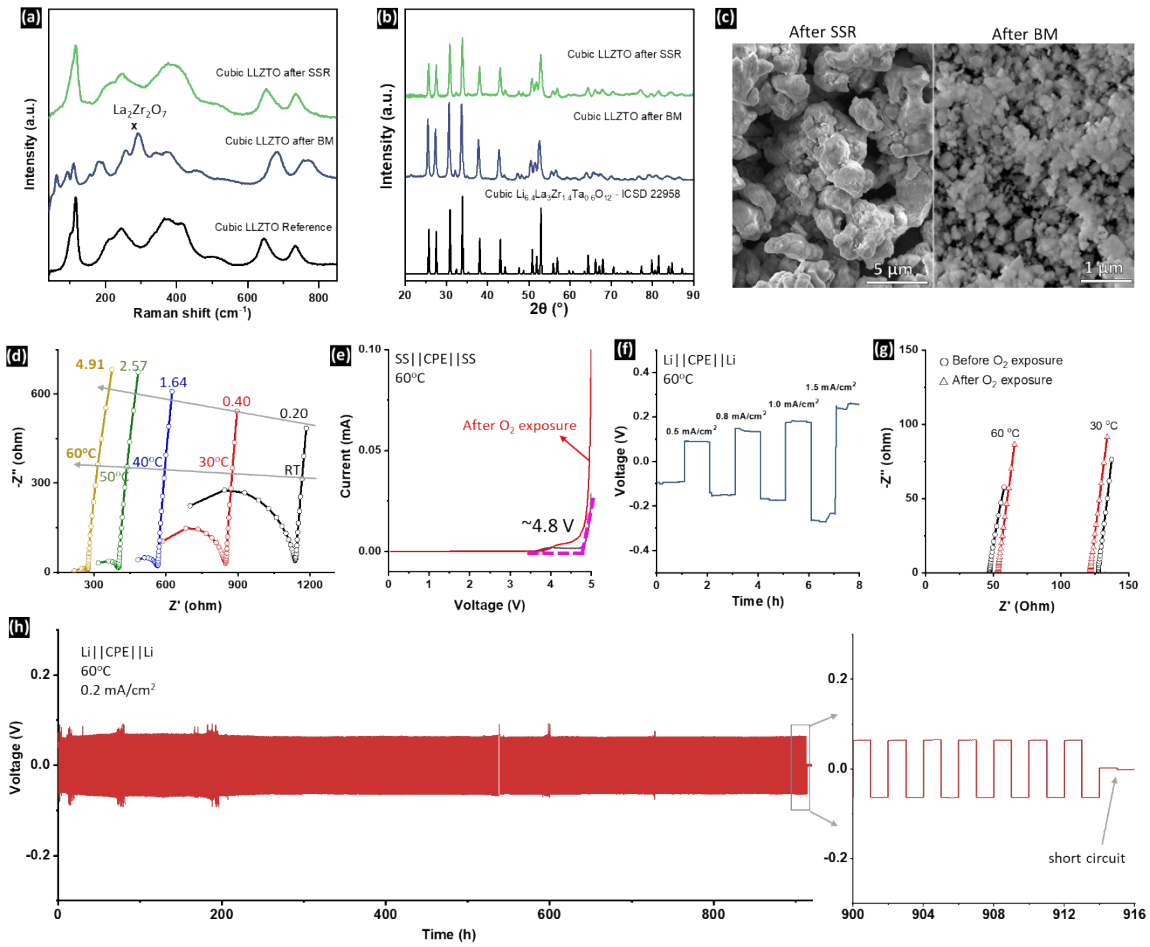

Figure S1. Structural and morphological characterization of LLZTO: (a) XRD patterns, (b) Raman spectra, and (c) SEM images after solid-state reaction and subsequent ball-milling. Electrochemical performance of the homemade CPE: (d) Nyquist plots at RT, 30 °C, 40 °C, 50 °C, and 60 °C, (e) LSV curve at a scan rate of 0.1 mV·s^{-1} before and after O_2 exposure, (f) Voltage-time profile of Li||CPE||Li symmetric cell at 0.5, 0.8, 1.0, 1.5 mA·cm^{-2}, (g) Nyquist plots of CPEs before and after O_2 exposure, (h) long-term cycling stability of Li||CPE||Li symmetric cell.

As shown in Figures S1a-c, cubic LLZTO was successfully obtained via solid-state reaction in a controlled flowing oxygen environment, and the particle size was reduced to below 300 nm after ball milling. Electrochemical performance of the homemade composite polymer electrolyte (CPE) is presented in Figures S1d-g. At room temperature (RT), the ionic conductivity is 0.20 mS·cm^{-1}, and it rises significantly to 4.91 mS·cm^{-1} at 60 °C. The LSV curve reveals an electrochemical stability window of 4.8 V for before and after O_2 exposure, which exceeds the cutoff voltage of the Li-O_2 batteries (2.0-4.5 V), indicating stability within the operational range. Under current densities of 0.5, 0.8, 1.0, and 1.5 mA cm^{-2}, the Li-stripping and plating process show relative low polarization at 60 °C, with corresponding voltages of ~90, 150, 180, and 250 mV, respectively. The long-term stability of CPE/Li was confirmed after cycling Li||CPE||Li symmetric cell for 912 hours.

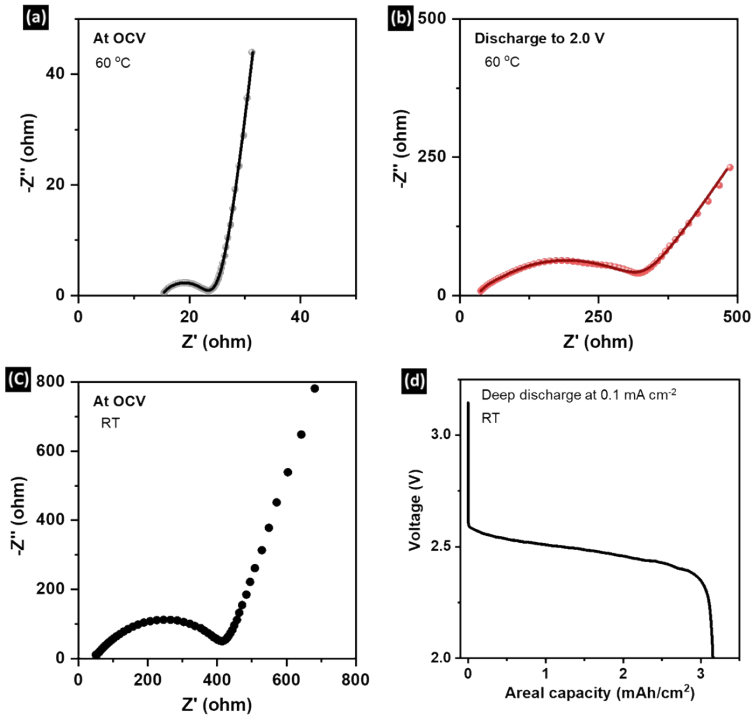

Figure S2. Nyquist plots of ASSLOB: (a) at OCV and (b) after discharge to 2.0 V at 60 oC. (c) Nyquist plots of ASSLOB at OCV and (d) corresponding discharge curve measured at room temperature.

The impedance spectra in Figure S2a,b were analyzed using equivalent circuit models:

At OCV, the spectrum was fitted using the model: $R_s + (R_{SEI}//CPE_{SEI}) + (R_{ct}//CPE_{ct}) + W_O$

where R_s is the series contact resistance; R_{SEI} and R_{ct} are the SEI resistance and the charge transfer resistance, respectively. CPE_{SEI} and CPE_{ct} are constant phase elements (CPEs) representing non-ideal capacitance at the SEI interface and for charge transport, while W_O denotes the Warburg coefficient.

After discharge to 2.0 V, the impedance spectrum exhibited multiple semicircles, indicating the presence of several overlapping processes. Three RC circuit elements were introduced to account for the major polarization processes: the SEI layer remained in the high-frequency range (10^5-10^4 Hz) and the charge transfer resistance appeared in the intermediate and low-frequency ranges (10^4-10^1 Hz). Accordingly, the equivalent circuit model was extended as:

$R_s + (R_{SEI}//CPE_{SEI}) + (R_{ct1}//CPE_{ct1}) + (R_{ct2}//CPE_{ct2}) + W_O$ (fully discharge to 2 V).

The EIS measurements performed at room temperature and at 60 °C are compared in Figure S2a and S2c. At room temperature, the markedly higher interfacial resistance and sluggish ion transport

severely hinder reaction kinetics, resulting in a reduced areal capacity of 3.2 mA·cm^{-2} (Figure S2d).

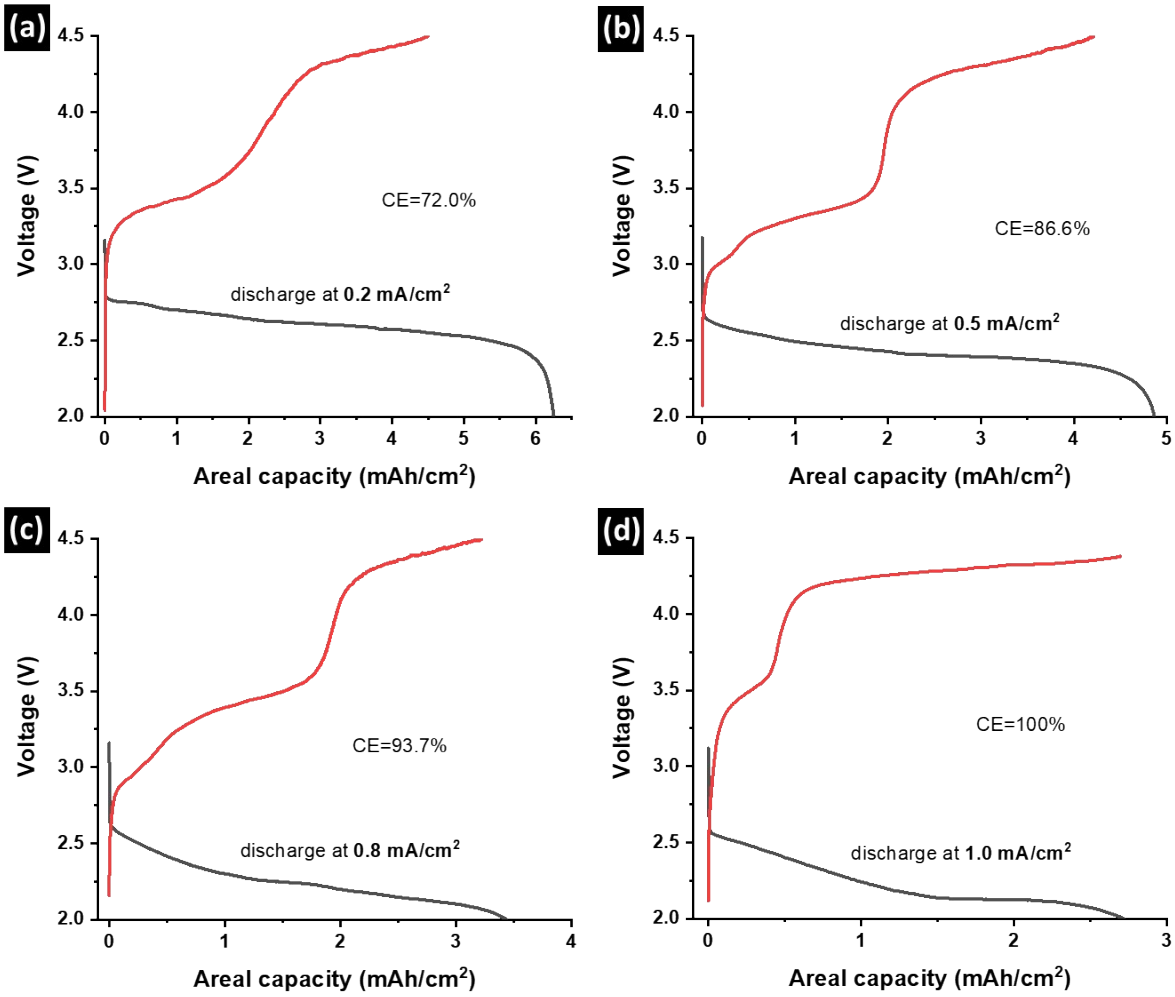

Figure S3. Discharge and charge profiles and the Coulombic efficiency (CE).

The discharged cells at the current densities of 0.2, 0.5, 0.8, and 1.0 mA·cm^{-2}, were recharged to 4.5 V at a current density of 0.1 mA·cm^{-2}, to evaluate the reversibility of ASSLOBs. The Coulombic efficiency was provided. At a higher discharge areal capacity, the CE is lower due to a thick and large amount discharge product. At a lower discharge areal capacity, a 100% CE was obtained suggesting that the discharge product can be fully decomposed.

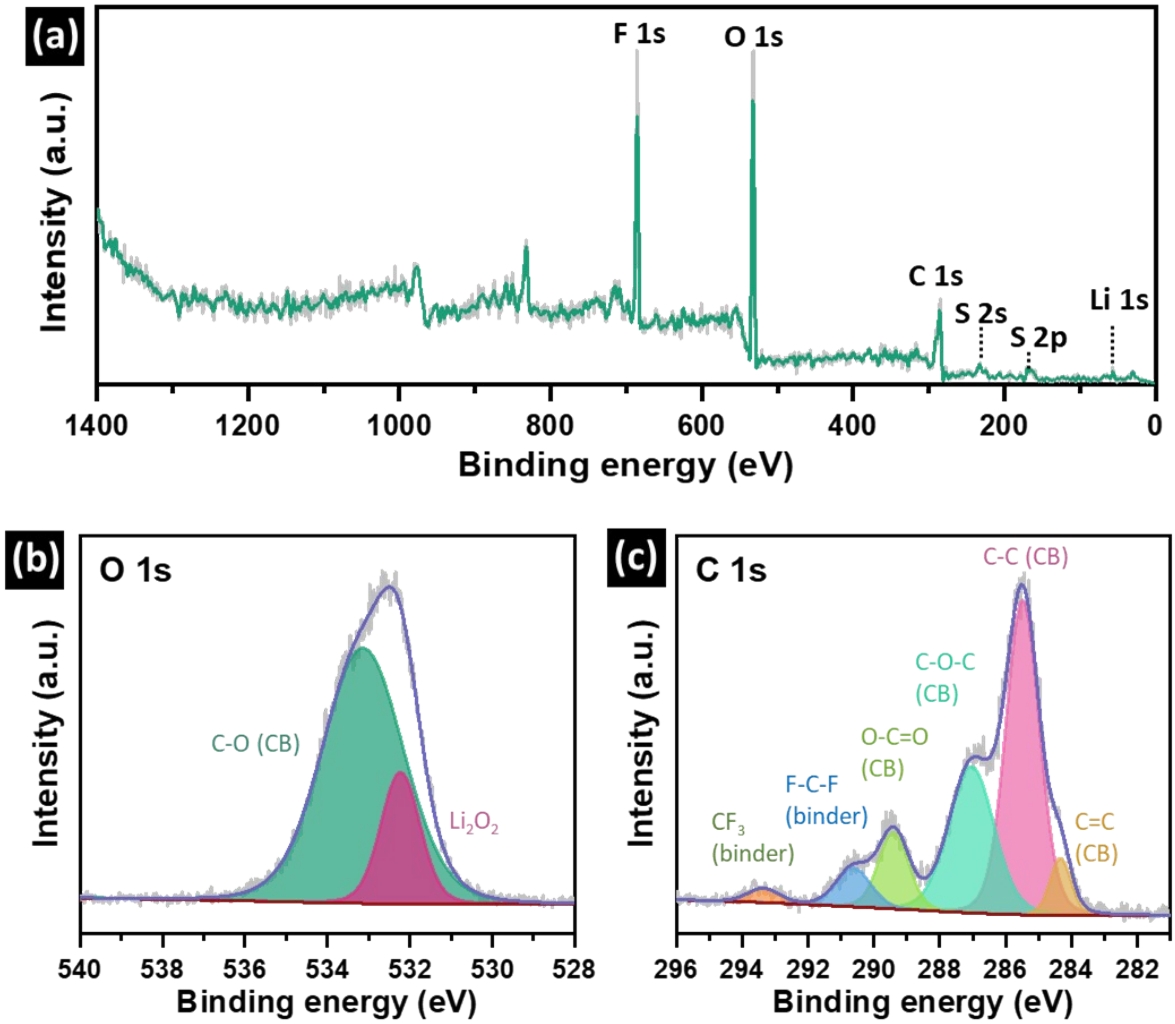

Figure S4. (a) XPS survey scan, (b) high-resolution O 1s, and (c) C 1s XPS spectra, calibrated with respect to the adventitious C 1 s peak at 284.8 eV.

The XPS survey scan shows signals corresponding to Li 1s (discharge product), S 2p and S 2s (both from Nafion), C 1s (majorly from carbon black), O 1s (discharge product and carbon black), and F 1s (binder). O1s exhibits a peak at 532.2 eV, corresponding to peroxide species in Li_2O_2, and a peak at 533.2 eV associated with organic C−O bonds, potentially arising from surface oxidation of carbon black (CB). C 1s shows signals at 284.3 eV and 285.5 eV, attributed to C=C and C–C bonds, respectively, which are linked to fused aromatic rings and graphitic carbon structures in CB. The PTFE binder may also contribute to the C–C signal, albeit to a lesser extent.

Peaks at 287.1 eV and 289.4 eV correspond to C–O–C (ether groups) and O–C=O (carboxyl groups), respectively, resulting from the substitution of carbon by oxygen and surface oxidation. The peak at 290.6 eV is assigned to C–F bonds from the PTFE binder, while the peak at 293.4 eV is attributed to $–CF_3$ (trifluoromethyl groups) from the Nafion binder additive.

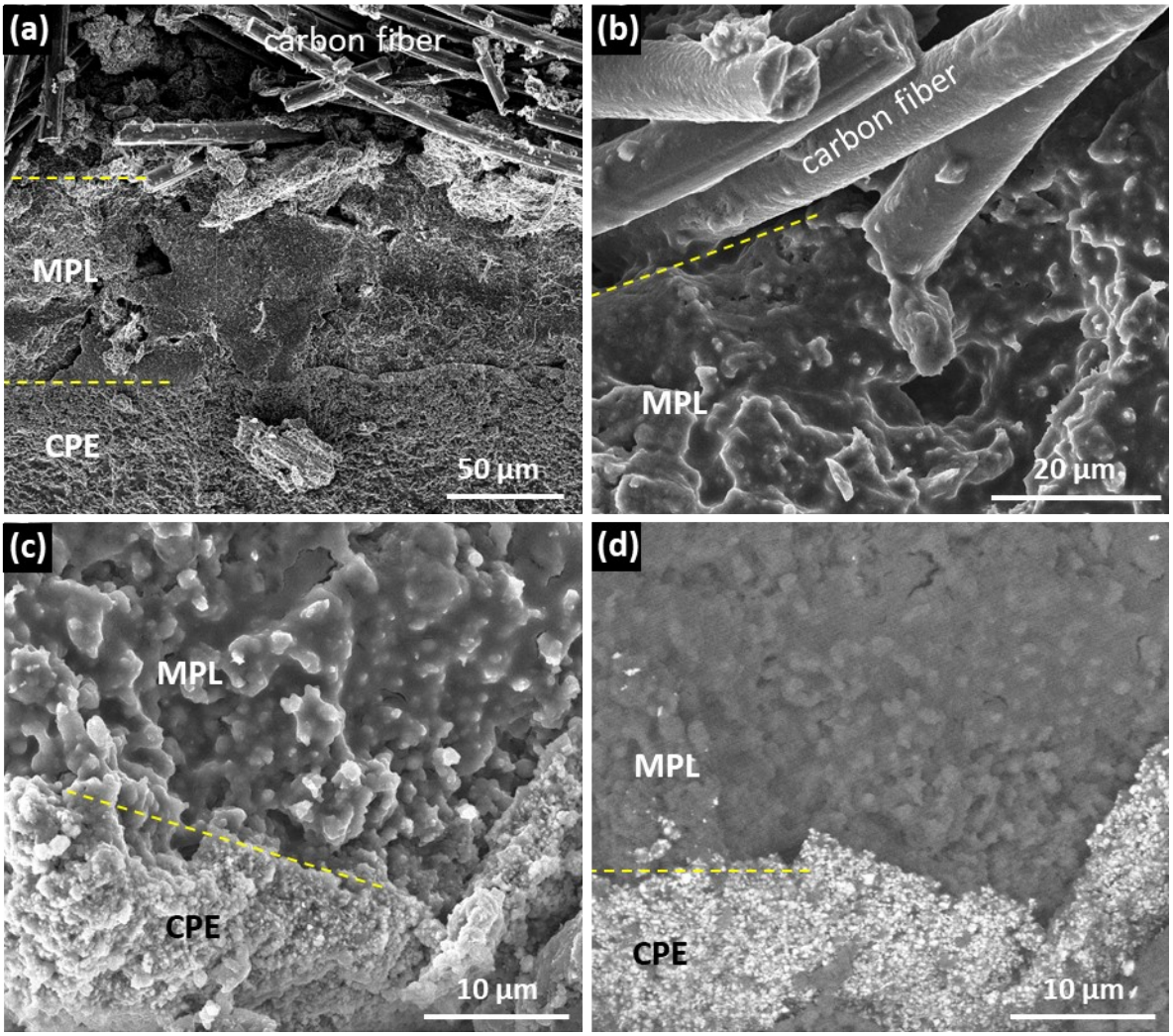

Figure S5. Cross-section SEM images showing intimate contact between CPE and MPL after discharged to 2.0 V: (a) Cross section of carbon cloth-MPL-CPE stacking. (b) carbon fiber and MPL interface. (c) MPL and CPE interface in secondary electron mode and (d) in backscattered electron mode.

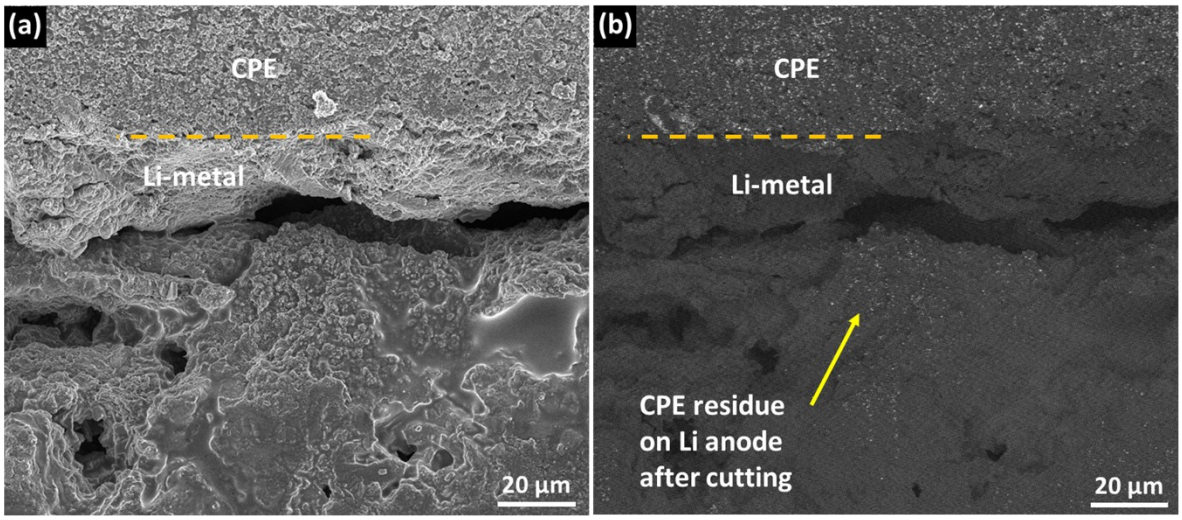

Figure S6. Cross-section SEM images showing intimate contact between CPE and Li-metal after discharged to 2.0 V.

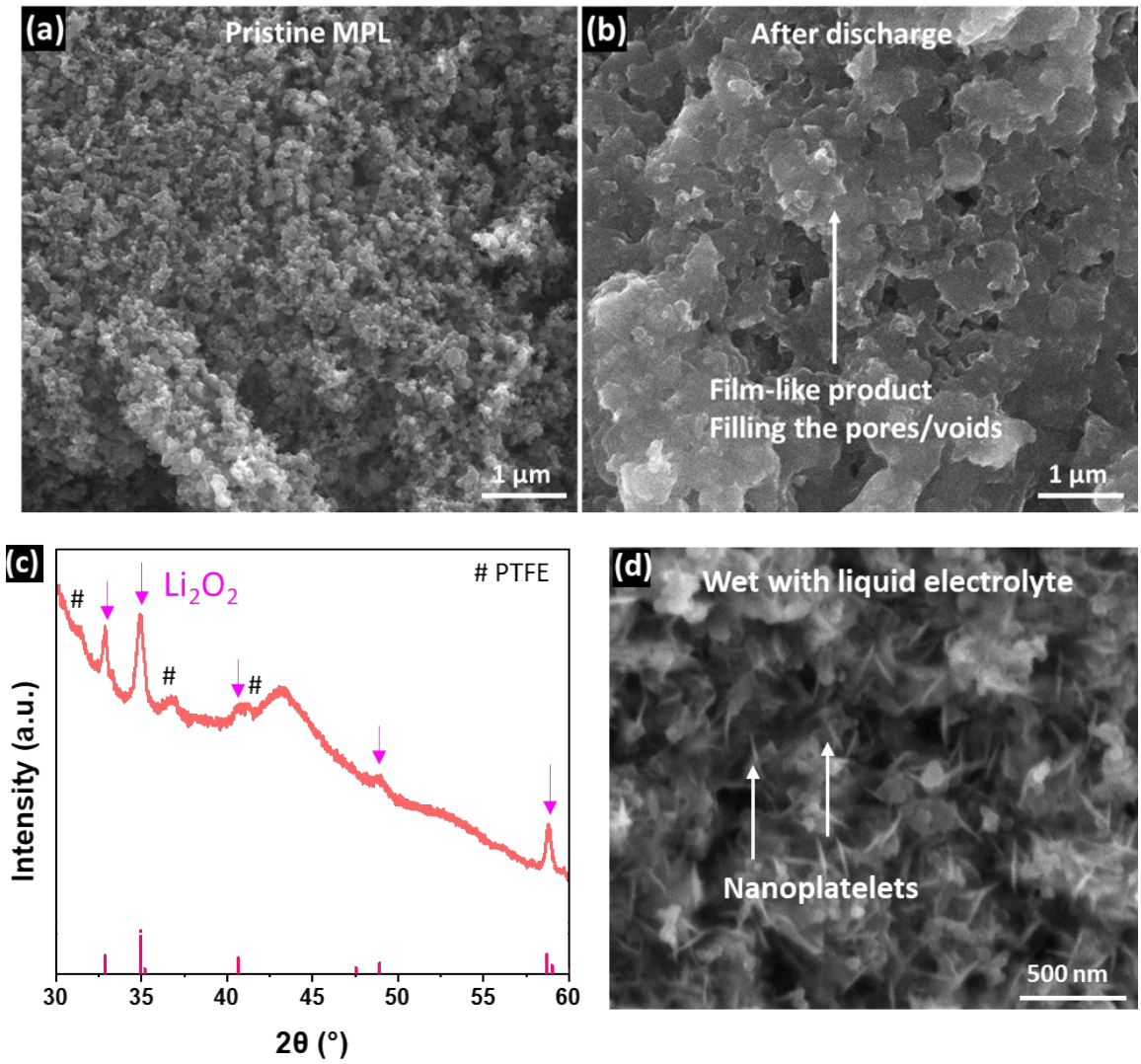

Figure S7. Microstructure of MPL comparison (a) before and (b) after discharge. (c) XRD patterns and SEM image of discharge product formed in the MPL under liquid electrolyte-wetted condition.

In Figure S7b, the SEM image shows film-like product coating on the surface of spherical carbon black particles and filling the interparticle pores and voids in MPL.As a result, the MPL becames denser compared with the pristine MPL. The influence of liquid electrolyte wetting on the crystal structure and morphology of the discharge product was further examined by XRD and SEM (Figure S7c,d). In contrast to the solvent-free configuration, the liquid-wetted MPL exhibits higher crystallinity and well-defined nanoplatelet morphologies. These results indicate that the presence of liquid electrolyte promotes solution-mediated crystal growth. In the present solvent-free system, we attribute the formation of amorphous, film-like discharge products to the combined effects of

(i) the absence of liquid solvent, which suppresses solution-mediated crystallization, and (ii) the large interfacial contact area provided by the gas-diffusion carbon cathode.

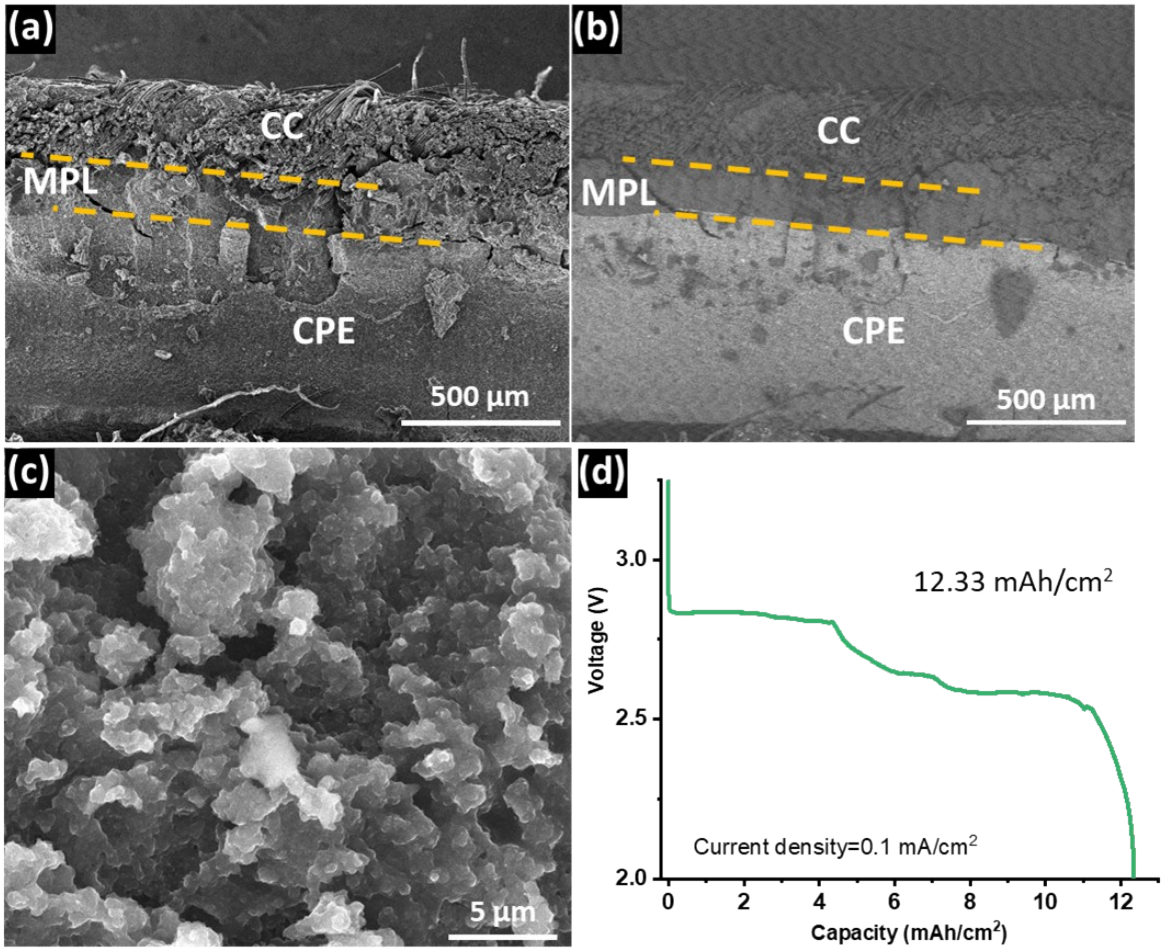

Figure S8. (a,b) Cross-section SEM images of the ASSLOB in the discharged state. (c) SEM image showing the morphology of the discharge product. (d) Discharge voltage profile at 0.1 $mA \cdot cm^{-2}$, corresponding to an areal capacity of 12.3 $mAh \cdot cm^{-2}$. *Note,* the thickness of homemade MPL is about 150 µm.

Increasing the MPL thickness from 50 to 150 µm increases the areal capacity from 6.33 to 12.33 $mAh \cdot cm^{-2}$ at 0.1 $mA \cdot cm^{-2}$.

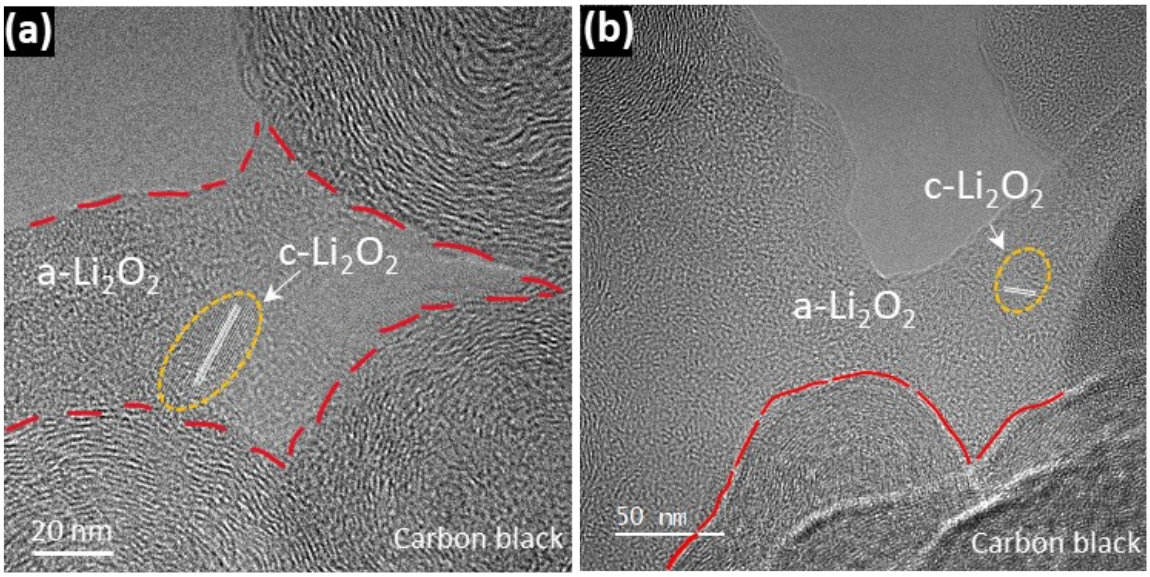

Figure S9. HRTEM images acquired at two different locations of the discharged MPL after resting in O_2 for one month, revealing crystalline Li_2O_2 (c-Li_2O_2) domains embedded within an amorphous Li_2O_2 (a-Li_2O_2) matrix.

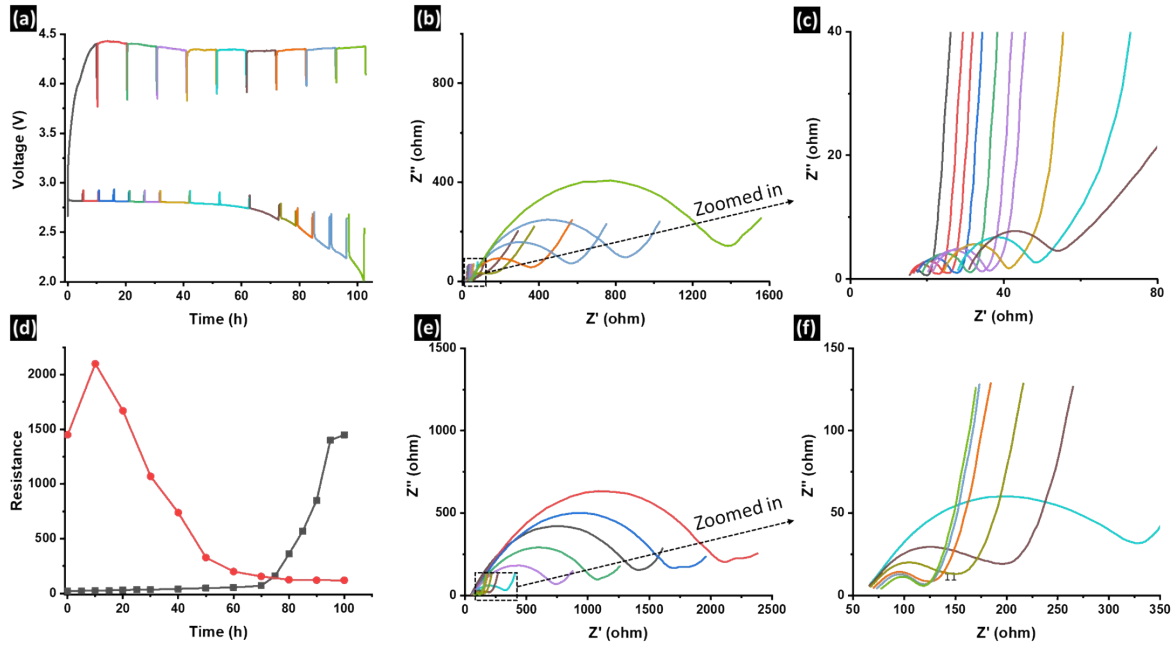

Figure S10. Operando EIS of ASSLOB. (a) Corresponding discharge/charge profiles at the current density of 0.05 mA·cm^{-2}. (b-c) Nyquist plots for discharge processes. (d) Summarized resistance evolution with discharge/charge time. (e-f) Nyquist plots for charge processes.

To study the dynamic formation and decomposition of discharge product within the porous cathode, operando Electrochemical Impedance Spectroscopy (EIS) was performed during discharge and charge at a current density of 0.05 mA·cm^{-2} over a voltage range of 2.0-4.5 V. The corresponding voltage profiles are shown in Figure S10a, with EIS collected at each step through the cycling process. The evolution of impedance as a function of discharge and charge time is summarized in Figure S10d. Notably, resistance contributions from different frequency regions change with the depth of discharge and state of charge, reflecting the complex interfacial and electrochemical processes.

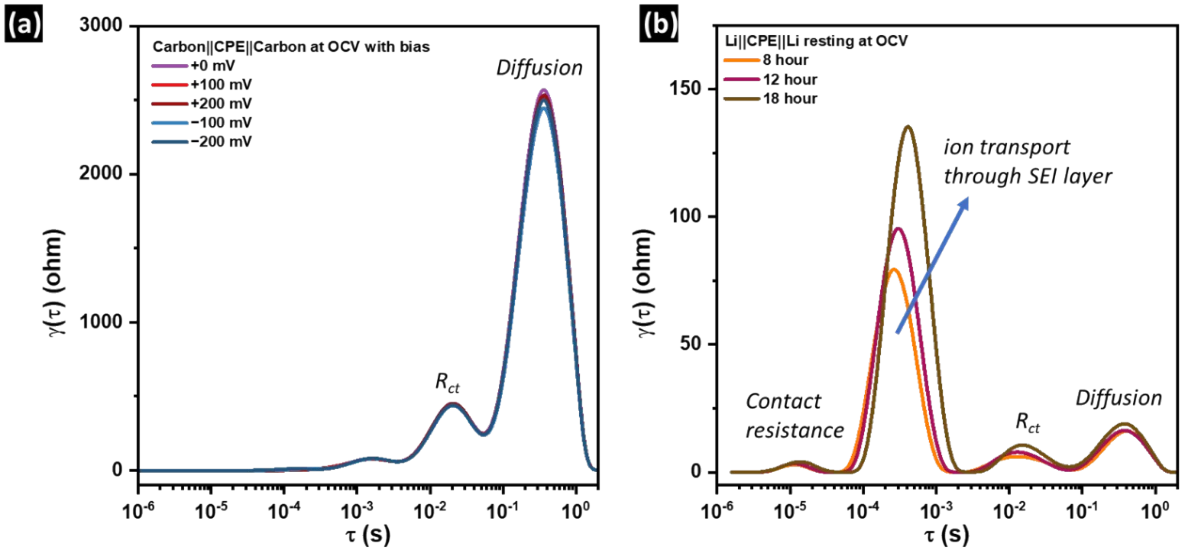

Figure S11. DRT analysis of (a) Carbon||CPE||Carbon and (b) Li||CPE||Li symmetric cells, measured at 65˚C in an Ar-filled environment, with (a) various overpotentials vs. OCV, and with (b) resting time of 8 h, 12 h, and 18 h at OCV.

DRT analysis of the Carbon||CPE||Carbon and Li||CPE||Li symmetric cells were performed to identify the frequency ranges associated with the charge transfer resistance at (Carbon-SSE interface) cathode and ion transport through SEI layer on the anode.

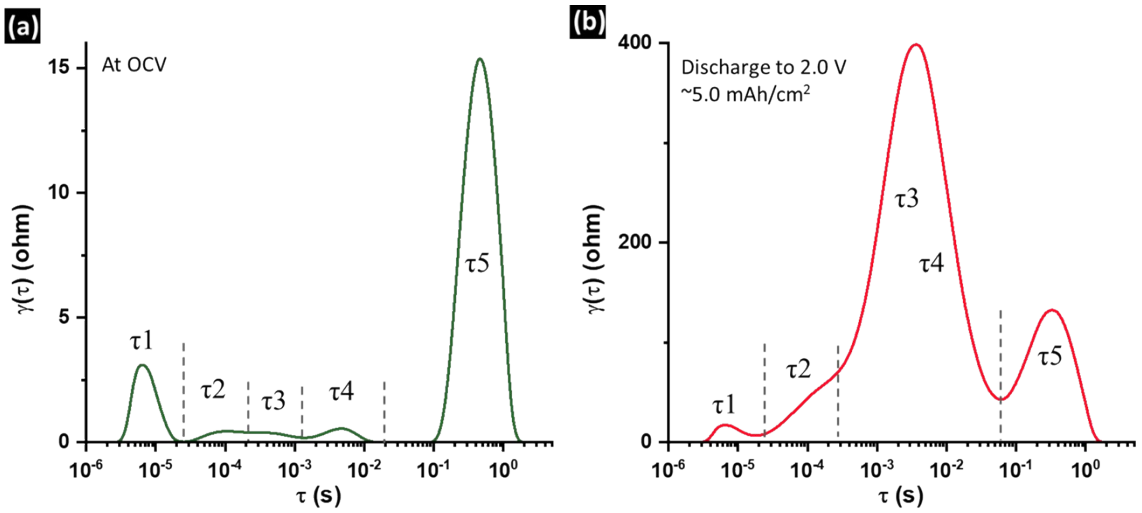

Figure S12. DRT analysis of ASSLOB: (a) at OCV before 1st discharging and (b) at the end of 1st discharging.

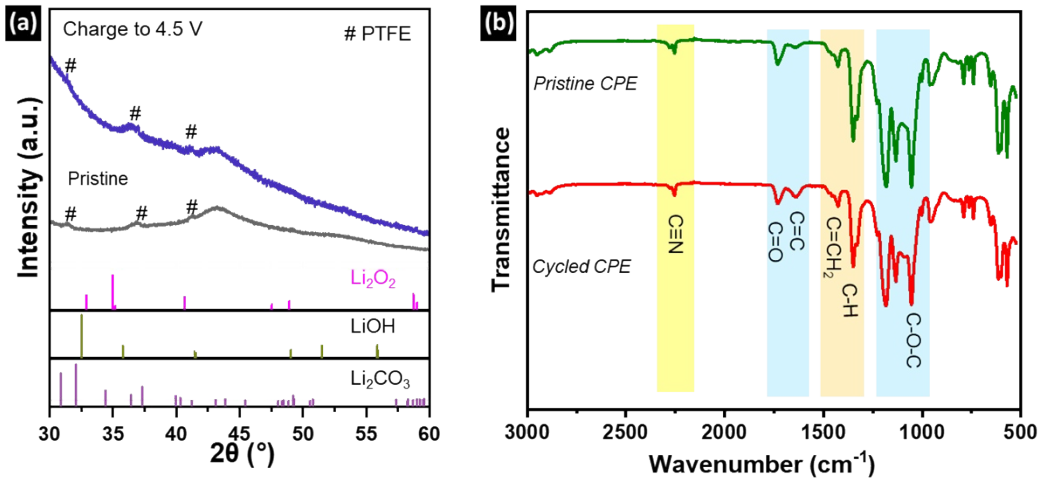

Figure S13. (a) XRD patten of gas-diffusion cathode after charged to 4.5 V and (b) FTIR spectra for CPE surfaces before and after cycling.

In Figure S13a, no Li_2CO_3 passivation layer or LiOH byproduct was detected on the gas-diffusion cathode after cycling and charging to 4.5 V.

In Figure S13b, FTIR spectra for CPE surfaces before and after cycling mainly display the spectroscopic characteristics of SCN and PEGDA, with no detectable new peaks associated with electrolyte decomposition or parasitic byproduct formation.

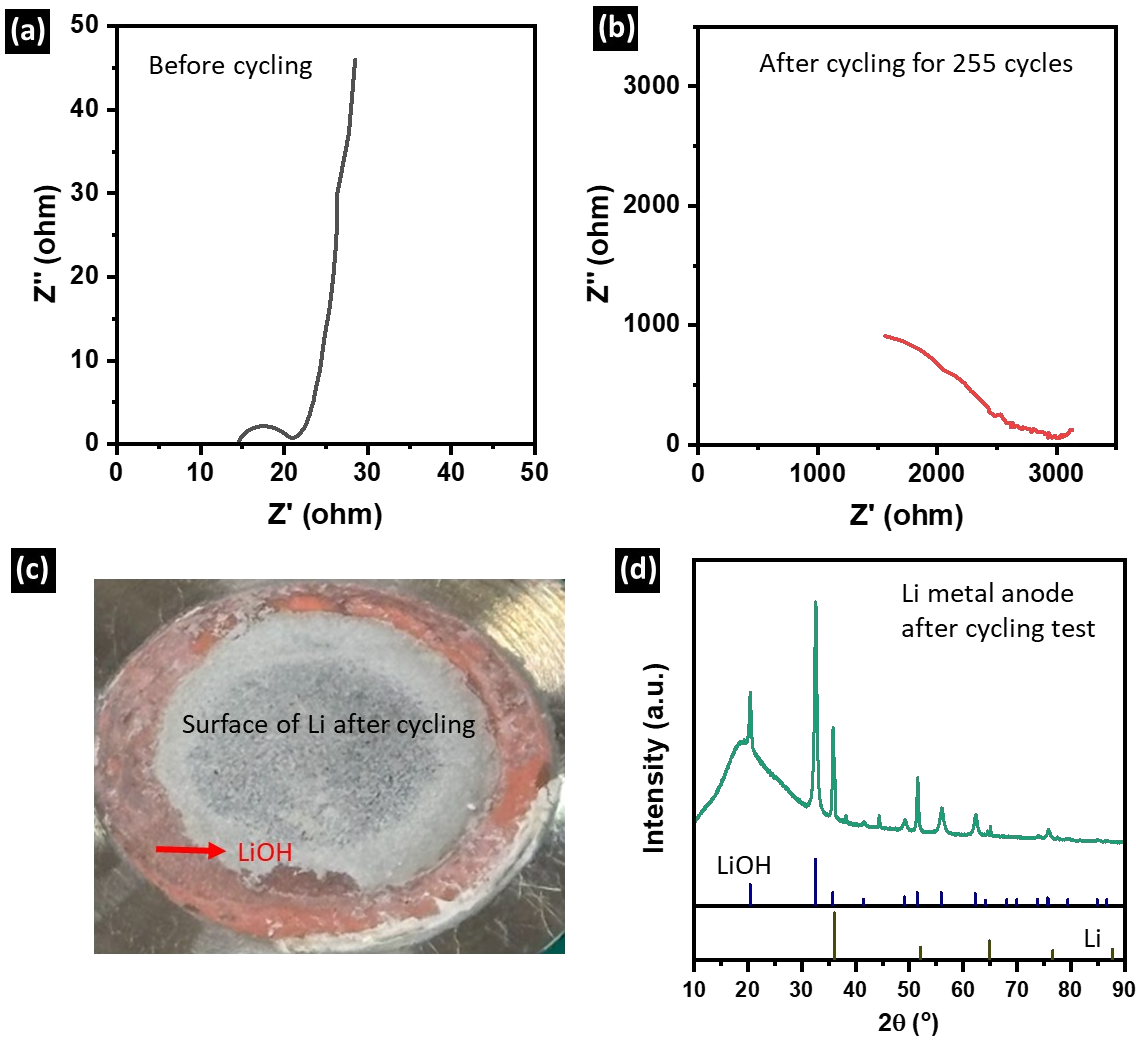

Figure S14. EIS of ASSLOB cell (a) before long-term cycling and (b) after 255 cycles (~510 hours) at a current density of 0.1 $mA \cdot cm^{-2}$. (c) Photograph showing Li metal corrosion after cycling. (d) XRD pattern of the cycled Li metal.

Table S1. Ionic and electronic properties of amorphous and crystalline Li_2O_2 reported in the literature

Reported Property	a-Li_2O_2	c-Li_2O_2
Ionic conductivity (S/cm)	7×10^{-8} (experimental)[46] 2×10^{-7} (computational)[44]	1×10^{-11} (experimental)[46] 4×10^{-19} (computational)[44]
Electronic conductivity (S/cm)	5×10^{-9} (experimental)[46] 2×10^{-16} (computational)[44]	1×10^{-13} (experimental)[46] 5×10^{-20} (in-plane, computational)[44] 1×10^{-24} (out of plane, computational)[44]

Table S2. (Quasi)-solid Li-O_2 systems: cathode structure, electrolyte type, operating condition, and cycling performance

Cathode structure	Electrolyte	Maxi-capacity	Cycling performance	Ref.
CB+Lithion binder coated on carbon cloth (0.72 mg/cm^2) adding LE electrolyte	Iongel soft PEGDM (10 wt.%) + ILE (LiTFSI+DEME-FSI, 90 wt.%)	2.62 mAh/cm^2 at 0.05 mA/cm^2 @60 ^{o}C	25 cycles with 0.2 mAh/cm^2 at 0.05 mA/cm^2	[30]
KB+PVDF/carbon paper adding LE (1M LiTFSI+0.05M LiBr in TEGDME)	PEGMEM+LiTFSI coated on Si-doped LAGP	7.3 mAh/cm^2 at 0.05 mA/cm^2	39 cycles with 0.4 mAh/cm^2 at 0.1 mA/cm^2	[31]
CNTs coated on SS mesh adding 1 μL cm^{-2} LE (0.5M LiTFSI in [C2C1im][NTf2]	Li-ion exchanged zeolite membrane (0.27 mS/cm at RT)	1.56 mAh/cm^2 at 0.065 mA/cm^2	149 cycles with 0.13 mAh/cm^2 at 0.065 mA/cm2	[23]
Ru-CNT+PVDF (9:1) coated on carbon paper (0.1 mg/cm^2)	Plastic crystal electrolytes (PCEs) (LiTFSI+PVDF-HFP+BHT+DMSO)	0.596 mAh/cm^2 at 0.02 mA/cm^2	130 cycles with 0.05 mAh/cm^2 at 0.02 mA/cm^2	[27]
CB+PVDF (9:1) coated on SS mesh (0.35 mg/cm^2)	Nafion membrine - 1M LiTSFI in TEDGME - PVDF-HFP	NA	56 cycles with 0.175 mAh/cm^2 at 0.035 mA/cm^2	[28]
CNT−Mn_3O_4−RuO_2	infiltration of PVDF-HFP-TEGDME-$LiClO_4$ into LLZTO	7540 mAh/g at 312.5 mA/g	194 cycles with 1250 mAh/g at 312.5 mA/g	[25]
CNT-film (1.0 mg/cm^2)	LiFSI+PVDF-HFP, solid polymer electrolyte (0.079 mS/cm at RT)	NA	60 cycles with 1.0 mAh/cm^2 at 0.4 mA/cm^2	[33]
Carbon + porous LAGP	LAGP (0.16 mS/cm)	0.48 mAh/cm^2 at 0.005 mA/cm^2	6 cycles with 0.08 mAh/cm^2 at 0.01 mA/cm^2	[21]
composite KB+LLZTO+LiTFSI+PPC (wt=6.3:6.3:6.3:1) (0.3166 mg/cm^2)	dense LLZTO pellet (relative density 99.6%) (1.6 mS/cm at RT)	6.43 mAh/cm^2 at 0.02 mA/cm^2 @80^{o}C	50 cycles with 0.3166 mAh/cm^2 at 0.02 mA/cm^2	[22]
SWCNT+ILE (LiTFSI in 1-ethyl-3-methyl imidazolium)	LAGP + PMS + SiO_2 + 1M LiTFSI in TEGDME with polyethylene as supporter	6.5 mAh/cm^2 at 0.1 mA/cm^2	350 cycles with 0.5 mAh/cm^2 at 0.1 mA/cm^2 at 50 ^{o}C 160 cycles with 0.5 mAh/cm^2 at 0.1 mA/cm^2 at RT	[32]
SWCNT+LAGP (0.176 mg/cm^2)	LAGP (0.2 mS/cm)	0.49 mAh/cm^2 at 0.035 mA/cm^2	10 cycles with 0.175 mAh/cm^2 at 0.07 mA/cm^2	[20]